Computational and Structural Biotechnology Journal 23 (2024) 4177–4191

Contents lists available at ScienceDirect

Computational and Structural Biotechnology Journal

journal homepage: www.elsevier.com/locate/csbj

Research article

# Ion and water permeation through claudin-10b and claudin-15 paracellular channels

Alessandro Berselli [a,b,c,1,2], Giulio Alberini [a,c,3], Fabio Benfenati [a,c,*,4], Luca Maragliano [a,d,**,5]

[a] Center for Synaptic Neuroscience and Technology (NSYN@UniGe), Istituto Italiano di Tecnologia, Largo Rosanna Benzi, 10, 16132 Genova, Italy
[b] Department of Experimental Medicine, University of Genova, Viale Benedetto XV 3, 16132 Genova, Italy
[c] IRCCS Ospedale Policlinico San Martino, Largo Rosanna Benzi, 10, 16132 Genova, Italy
[d] Department of Life and Environmental Sciences, Polytechnic University of Marche, Via Brecce Bianche, 60131 Ancona, Italy

ARTICLE INFO

*Keywords:*
Claudin-10b
Claudin-15
Tight junction
Molecular dynamics simulations
Water permeability
Free energy calculations

ABSTRACT

The structural scaffold of epithelial and endothelial tight junctions (TJs) comprises multimeric strands of claudin (Cldn) proteins that anchor adjacent cells and control the paracellular flux of water and solutes. Based on the permeability properties they confer to the TJs, Cldns are classified as channel- or barrier-forming. For instance, Cldn10b, expressed in kidneys, lungs, and other tissues, displays high permeability for cations and low permeability for water. Along with its high sequence similarity to the cation- and water-permeable TJ protein Cldn15, this makes Cldn10b a valuable test case for investigating the molecular determinants of paracellular transport. In lack of high-resolution experimental information on TJ architectures, here we use molecular dynamics simulations to determine whether atomistic models recapitulate the differences in ion and water transport between of Cldn10b and Cldn15. Our data, based on extensive standard simulations and free energy calculations, reveal that Cldn10b models form cation-permeable pores narrower than Cldn15, which, together with the stable coordination of $Na^+$ ions to acidic pore-lining residues (E153, D36, D56), limit the passage of water molecules. By providing a mechanism driving a peculiar case of paracellular transport, these results provide a structural basis for the specific permeability properties of Cldn subtypes that define their physiological role.

## 1. Introduction

The movement of water, ions, and molecules across epithelia or endothelia occurs by following distinct transcellular and paracellular pathways. The former involves specific channels or transporters [1–4], while the latter relies on passive diffusion through the narrow space between adjacent cells, regulated by a meshwork of multiprotein strands hinging cells together and named tight junctions (TJs) [5–7]. The TJ backbone is formed by multimers of claudin (Cldn) proteins that determine the selective permeability of the strands to electrolytes and

*Abbreviations:* APBS, Adaptive Poisson-Boltzmann solver; Cldn, Claudin; COM, Center of mass; CV, Collective variable; CZAR, Corrected z-averaged; ECH, Extracellular helix; ECL, Extracellular loop; FE, Free energy; GBIS, Generalized-Born implicit solvent; HMR, Hydrogen-mass repartitioning; JDR, Joined-double row; MD, Molecular dynamics; PME, Particle-mesh Ewald; POPC, 1-palmitoyl-2-oleoyl-sn-glycero-3-phosphocholine; RMSD, Root-mean square deviation; TAL, Thick ascending limb; TAMD, Temperature-accelerated molecular dynamics; TJ, Tight junction; TM, Transmembrane helix; US, Umbrella sampling; VdW, Van der Waals; WHAM, Weighted-histogram analysis method.

* Corresponding author at: Center for Synaptic Neuroscience and Technology (NSYN@UniGe), Istituto Italiano di Tecnologia, Largo Rosanna Benzi, 10, 16132 Genova, Italy.
** Corresponding author at: Department of Life and Environmental Sciences, Polytechnic University of Marche, Via Brecce Bianche, 60131 Ancona, Italy.
*E-mail addresses:* fabio.benfenati@iit.it (F. Benfenati), l.maragliano@staff.univpm.it (L. Maragliano).
[1] Present address: Department of Chemical and Geological Sciences (DSCG), University of Modena and Reggio Emilia (UNIMORE), Via Campi 103, 41125 Modena, Italy.
[2] ORCID: https://orcid.org/0000-0002-2241-3530
[3] ORCID: https://orcid.org/0000-0003-2794-2084
[4] ORCID: https://orcid.org/0000-0002-0653-8368
[5] ORCID: https://orcid.org/0000-0002-5705-6967

https://doi.org/10.1016/j.csbj.2024.11.025
Received 15 September 2024; Received in revised form 9 November 2024; Accepted 10 November 2024
Available online 13 November 2024

molecules in a tissue-specific manner [8–10]. Structurally, Cldns are folded in a transmembrane four-helix bundle (TM1–4), linked to each other by two loops in the paracellular space (ECL1–2) and one intracellular loop (ICL) in the cytosol, where the N- and C-termini are also found [11–14]. The ECL1 is typically composed of ~ 50 amino acids and comprises a four-stranded $\beta$-sheet ($\beta$1–4), along with a highly conserved extracellular helix (ECH). The ECL1 domain is crucial for the formation of the intercellular Cldn-Cldn *trans*-interactions and includes the amino acids responsible for the TJ charge-selective permeability. The ECL2 is shorter (< 30 amino acids), provides a fifth $\beta$-strand ($\beta$5) to the extracellular five-stranded $\beta$-sheet, and is essential for the stabilization of the *cis*- interactions between monomers in the same cell [15,16].

The family of mammalian Cldns includes 27 members [12,17], that can be classified based on their physiological function as channel-forming or barrier-forming. For example, Cldn2 [18], Cldn10b [19,20], Cldn15 [21], Cldn16 and Cldn19 together [22,23], and Cldn21 [24] form cation-permeable systems, while Cldn10a [25] and Cldn17 [26] are selective to anions. Conversely, a barrier function was demonstrated for Cldn1 [27], Cldn3 [28], Cldn5 [29], Cldn11 [30] and Cldn14 [31]. The evaluation of TJ water permeability is generally more controversial, given the difficulties in determining how the paracellular and transcellular routes contribute to the total transepithelial flux [32]. For the kidney proximal tubule, the relative contributions have been provided [33,34], resulting in about 30 % paracellular mainly conveyed by Cldn2-based TJs. Cldn15 also exhibits water permeability [35,36], whereas Cldn17 [26], Cldn10a, and Cldn10b do not [32,36]. The latter is largely expressed in the water-impermeable regions of the kidney's Henle's loop [37], and is particularly interesting because it shows high sequence similarity to the water-permeable Cldn15. In light of these properties, a current classification further distinguishes channel-forming Cldns in: (i) cation and water channels (Cldn2 and Cldn15), (ii) cation channels (Cldn10b and Cldn16/Cldn19), and (iii) anion channels (Cldn10a and Cldn17) [38].

While the structures of several Cldn monomers have been obtained experimentally, no detailed information on how they associate to form TJs is currently available. A model was suggested years ago [39], based on the Cldn15 monomeric crystal structure (PDB ID: 4P79 [40]). The architecture displays two patterns of protein-protein interactions between monomers from the same cell, named *cis-linear* and *face-to-face* [41]. The *cis-linear* arrangement generates single filaments of Cldn monomers, while *face-to-face* interactions join two antiparallel filaments in a double-row, where the ECL $\beta$-strands of each couple of Cldn15 monomers form a peculiar "*half pipe*"-shaped structure [39]. When double-row strands from neighbor cells *trans*-associate, the "*half pipes*" are joined, resulting in $\beta$-barrel pores parallel to the facing cell membranes. This architecture is referred to as the Suzuki, or joined-double row (JDR) [14] model, and is consistent with cross-linking experiments and freeze-fracture electron microscopy. It was refined and validated using molecular dynamics (MD) simulations first for Cldn15 [42–45], and then for several other homologs [46–53]. In our previous MD studies, we assessed it by calculating the free energy (FE) of ion permeation through single-pore Cldn tetramers, considering these as the minimal functional units of the model. Other groups analyzed higher-order multimers and reproduced ionic currents flowing through the pores [44,50]. Altogether, these works showed that the model correctly reproduces the experimentally determined ion selectivity of various Cldns, which stems from the electrostatic environment generated by the pattern of charged pore-lining residues.

In this study, we use all-atom MD simulations and FE calculations to determine whether the JDR model adequately captures the cation selectivity and low water permeability of Cldn10b. We employ two variants of a triple-pore multimer and compare the results with those obtained for Cldn15. The two models differ by the orientation of the $\beta$1$\beta$2 loop (between the $\beta$1 and $\beta$2 strands of each monomer) that is not present in the original JDR structure, resulting in distinct orientations of critical pore-facing residues. Model1 is based on the Cldn15 double-pore conformation we previously published [43], while Model2 has been proposed by Piontek and collaborators [50,51].

Standard MD simulations on the microsecond timescale show that both Cldn10b JDR models are cation-selective and less water permeable than Cldn15, consistent with experimental findings. Water passage is hindered by the small size of the pores (~ 2.2 Å of minimal radius) and the clustering of cations within the cavities. FE calculations result in repulsive barriers for $Cl^-$, attractive minima for cations, and barriers for water whose height depends on the number of $Na^+$ ions occupying the pore. These outcomes support the validity of the JDR model and provide insight into the structural and molecular determinants of the transport of ions and water through Cldn-based channels, describing a novel mechanistic perspective of the paracellular transport.

## 2. Materials and methods

### 2.1. Construction of the Claudin-10b and Claudin-15 multi-pore models

We built two Cldn10b JDR models, each comprising three adjacent pores. The first one, Model1, was generated using an equilibrated configuration of the Cldn15 double-pore system we produced before as a template [43]. From this model, we extracted four Cldn15 monomers forming the interface between two adjacent pores (Fig. S1). One of the Cldn15 units was used as a template to model the Cldn10b monomer with SWISS-MODEL [54]. Then, four replicas of the resulting monomer were superimposed on the Cldn15 ones. Major clashes were solved using GalaxyRefineComplex [55], and the resulting configuration was replicated to form a dodecameric triple-pore system with the help of VMD [56]. Finally, the four most external protomers were added to preserve the *cis*-interactions of each protein. The final hexadecameric multimer was relaxed with the Generalized-Born Implicit Solvent (GBIS) method [57,58]. The cutoff for the VdW interactions was set to 14 Å and the time step was 2 fs. After a starting minimization, 15 ns of equilibration were performed with NAMD3 [59] and the CHARMM36m [60] force field.

The second Cldn10b triple-pore model, here named Model2, corresponds to the *octameric interlocked barrel* configuration resulting after 100 ns of MD simulations produced by the group of Dr. Piontek (see Nagarajan et al. [51]).

Finally, the Cldn15 tetra-pore system was generated via the same procedure described for Cldn10b Model1.

### 2.2. Assembly of the systems

Each Cldn10b and Cldn15 multi-pore was translated in order to move its center of mass (COM) onto the origin of the reference system in VMD [56]. The axis of the central paracellular pore was oriented parallel with the Cartesian *y*-axis. Two hexagonal membranes of pure 1-palmitoyl-2-oleoyl-glycero-3-phosphocholine (POPC) were generated using the *membrane builder* tool of CHARMM-GUI [61,62] and equilibrated separately for 10 ns with the NAMD3 software [59] and the CHARMM36 [60] force field using hexagonal periodic boundary conditions. Then, the systems were embedded into the equilibrated double membrane bilayer and solvated with TIP3P water molecules [63] and a physiological NaCl ionic bath (0.15 M). The final boxes are hexagonal prisms with a base inscribed in a square of approximately 200.0 × 200.0 $Å^2$ and a height of about 160.0 Å, counting ~ 500,000 atoms (Fig. 1). The topology file was built with the *psfgen* tool of VMD [56], using the parameters of the CHARMM36 [60]/ CHARMM36m [64–66] force field. Disulfide bridges between residues C53 and C63 in the ECL1 of each protomer were preserved for both Cldn10b and Cldn15 proteins.

### 2.3. Equilibration and standard MD simulations

All systems were equilibrated with a multi-step protocol comprising a progressive release of harmonic restraints on heavy atoms (Table S1). After a first energy minimization, 100 ns of equilibration and 1000 ns of

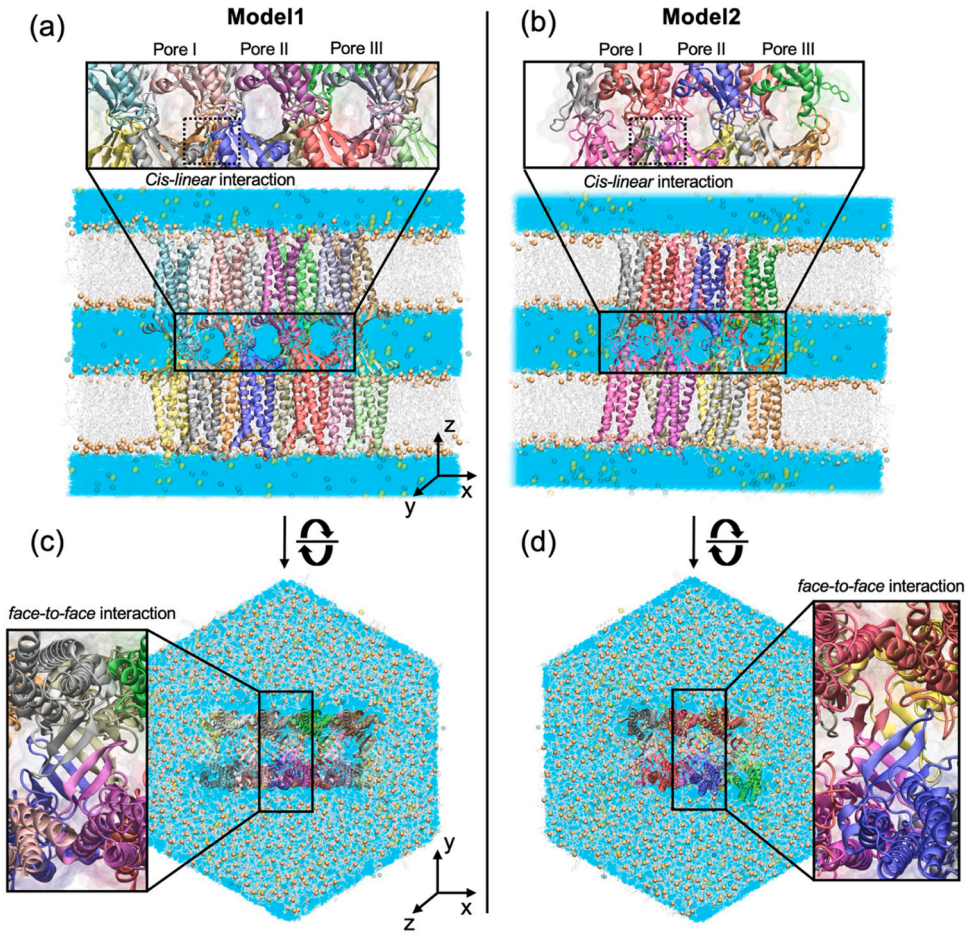


**Fig. 1.** Claudin-10b triple-pore models. (a,b) Apical views of the Cldn10b triple-pore Model1 and Model2 structures, respectively. Close-up views of the ECL domains are shown, with the cis-linear interactions indicated with a dotted square. (c,d) Lateral views of Model1 and Model2. Close-up views of the face-to-face interaction are included. The proteins are embedded in a hexagonal double membrane lipid bilayer (hydrophobic lipid tails are shown as grey sticks, lipid phosphorous atoms as orange spheres), solvated with water (cyan) and NaCl ionic bath (blue and yellow spheres). The starting configuration of each system (after minimization) is shown.

production were carried out in the NPT ensemble at a constant temperature and pressure of 310 K and 1 bar, respectively. To this aim, a Langevin thermostat and Nosé -Hoover Langevin piston [67,68] were used. Following the setup suggested by the CHARMM-GUI configuration files for NAMD [61], the oscillation piston period was set to 50.0 fs and the damping time scale to 25.0 fs. The damping coefficient of the Langevin thermostat was set to 1 $ps^{-1}$. Electrostatic and van der Waals (VdW) interactions were calculated with a cutoff of 12 Å as customary with the CHARMM force field. A switching function was applied starting to take effect at 10 Å to obtain a smooth decay [69]. Long-range electrostatic interactions were computed using the Particle-Mesh Ewald (PME) algorithm [70], with spline interpolation order 6. A maximum space between grid points of 1.0 Å was used. Chemical bonds between hydrogen atoms and heavy atoms were constrained with SHAKE [71], while those of the water molecules were kept fixed with SETTLE [72]. A time step of 1 fs was employed for the first 20 ns of equilibration. Then, it was increased to 2 fs for the subsequent 80 ns, re-initializing all atomic velocities after every 10 ns. The production phase was conducted maintaining the same restraints on the C$\alpha$ atoms belonging to the TM helices as the last equilibration step, mimicking the constraining effect of the adjacent protomers in the strands. In Model1, the ECLs of the four most external protein monomers were also restrained. One replica of each Cldn10b system and the one for Cldn15 were simulated using a timestep of 2 fs. Two other replicas of each Cldn10b model were simulated using the hydrogen-mass repartitioning (HMR) method [73–75], adopting a time step of 4 fs. In HMR, the mass of hydrogen atoms not belonging to water molecules is adjusted to 3.024 amu, and those of the covalently bound heavy atoms are proportionally scaled down so that the total mass of the system is conserved. In these simulations, as suggested in Ref. [73], the oscillation period of the Langevin piston period was set to 300 fs, while the damping time scale was 150 fs. MD simulations were performed with NAMD3 [59]. The CHARMM36/-CHARMM36m [64–66] parameters were used to simulate the lipids and the proteins, respectively. The TIP3P model for water molecules [63] and the associated ionic parameters with NBFIX corrections [76–78] were employed.

### 2.4. Analysis of the standard MD simulations

*Root-mean square deviations.* We calculated the root-mean square deviation (RMSD) of the backbone atoms of all paracellular domains formed by the Cldn10b ECLs (residues 28 to 73 and 149 to 161 of each monomer). The analysis was conducted along the simulated trajectories of each replica with the help of VMD [56] and the Tcl scripting interface. For each Cldn10b model, RMSD averages and errors were calculated using the three simulations.

*Pore radii.* The size of the paracellular pores was calculated using HOLE [79,80]. This program maps the radius of a protein cavity along a given axis (the *y*-axis, in this case) by fitting a spherical probe in the space not occupied by the VdW spheres of the pore-lining atoms. A maximum value of 15 Å was chosen as a threshold for all systems. Radius values of each Cldn10b system were calculated for the central pore every 50 ns of the replicated trajectories.

*Electrostatic surfaces.* Electrostatic potential maps were computed

with the adaptive Poisson-Boltzmann solver (APBS) code [81], using the default parameters set by the developers.

*Cross-distances.* Cross-distances between representative residues belonging to the central pore were calculated with Tcl in VMD [56]. The distances consider the most external C-atom of the sidechain in the case of aliphatic amino acids, or the center of mass of the benzene ring in the case of aromatic residues.

*Number of water/ion permeation events.* The number of water molecules or ions crossing the central paracellular cavity during the simulated trajectories was calculated with VMD [56] and an *in-house* Tcl script. We defined two 20 Å-thick disk-shaped regions at the two entrances of the pore, named disk1 and disk2, with radii comparable to the pore size. At each simulation step, we tagged all water molecules and ions inside each disk, creating two separate lists. The trajectories of these particles were monitored by tracking their *y* coordinates, and a permeations event was counted when one of them crossed disk2 coming from disk1 (or vice-versa), excluding transitions by periodic boundary conditions. If a particle leaved the cavity by any direction, it was removed from the pertaining list. At each iteration, the lists of particles inside the two disks are updated.

*Ion hydration spheres*. The number of water molecules in the hydration shell of $Na^+$ ions inside the central pore was calculated with VMD [56] and Tcl by setting a cutoff to the distance between the ion and the water's oxygen atom of 3.0 Å, in agreement with the value determined in Ref. [82].

*Number of water-protein hydrogen bonds*. The HBs formed between water molecules and the pore-lining residues were calculated inside the central pore of both Cldn10b and Cldn15. We split the pore axis into 60 bins of 1 Å and, in each of them, we determined the number of HBs by adopting a distance cutoff of 3.3 Å between the donor H and the acceptor X and an angle cutoff of 150° between X-H—X, where X is a heteroatom (O, N or S for the protein, O for water). This calculation was repeated for each replica of the systems, sampling the trajectories every 10 ns and the average HBs number and standard deviation were calculated for each bin.

### 2.5. Free energy calculations

*Umbrella Sampling simulations.* The free energy (FE) profiles of water and ion permeation were calculated with Umbrella Sampling (US) [83], with the same setup we adopted in previous works [42,43,47,48,84] and the Colvars module [85]. Accordingly, one single collective variable (CV) was considered, represented by the *y* coordinate of the tagged ion or water molecule that permeated the central paracellular cavity. A summary of the US simulations is reported in **Section S1**. Before the production phase, each US window was energy-minimized and equilibrated in two steps, performing 1 ns with a time step of 2 fs, followed by 1 ns with a time step of 4 fs and the HMR setup. Then, each window was simulated under HMR, with all details specified for the standard MD simulations, until convergence was achieved. For water, a 40-ns window was required, while 60 ns and 80 ns per window were carried out for both cations and $Cl^-$, respectively, resulting in a total of $\sim 17$ $\mu$s per each Cldn10b model. In the case of the calculations of water permeation with one (for Model1) or three (for Model2) $Na^+$ ions coordinated inside the cavity, each cation was restrained between opposing pairs of acidic residues (one D56 pair for Model1, two D36 pairs and one D56 pair for Model2). We used the Colvars module to implement the half-harmonic restraints with constants of 1 kcal/(mol • $Å^2$) starting to take effect at a distance between the ion and both the two facing carboxylic sidechains $> 8$ Å. For these calculations, each window was simulated for 60 ns, corresponding to a total of $\sim 4.2$ $\mu$s per each Cldn10b model. Finally, the FEs were obtained by combining the CV distributions of all windows using the weighted-histogram analysis method (WHAM) [86–88]. To this aim, we employed the code from the Grossfield group available at http://membrane.urmc.rochester.edu/content/wham.

*Temperature-accelerated Molecular Dynamics simulations.* The FE profiles of water permeation through the cavities of Cldn10b triple-pores occupied by the number of $Na^+$ ions suggested by standard MD simulations were computed using temperature-accelerated molecular dynamics (TAMD) [89,90]. A detailed description of TAMD is provided in **Section S2**. As in the case of US calculations, the chosen CV is the *y* coordinate of the tagged water molecule passing through the central cavity of the system. The CV-axis was split into three windows spanning from −35 Å to −10 Å, from −10 Å to 10 Å, and from 10 Å to 34 Å. Each window was equilibrated with the same procedure used for the US calculations and simulated for 200 ns under the same conditions as the standard MD simulations and adopting the HMR setup. An effective temperature $\overline{T}= 1000$ K and an effective friction $\overline{\gamma} = 10$ $ps^{-1}$ were used for the CV's dynamics. The FE calculations were performed by constraining six or eight ions inside the central cavity of the Cldn10b triple-pores using Colvars [85]. We adopted a harmonic constant of 10 kcal/mol starting to take effect at the extremities of the pore, for $y < -35$ Å and $y > 34$ Å. The instantaneous force on the CV was collected in bins of 0.1 Å, and the FE was computed by integrating the average force with the corrected z-averaged (CZAR) estimator [91]. The resulting profile and the associated error were reported as the mean and the standard deviation from two replicas. To assess the consistency between the results produced by US-WHAM and TAMD calculations, we repeated the single-ion calculations of $Na^+$ permeation through the Model2 central cavity by adopting the setup described above. The comparison between the FE curves obtained with the two methods is reported in Fig. S2.

## 3. Results

### 3.1. Claudin-10b models are stable during MD simulations and exhibit different orientations of pore-lining residues

The two Cldn10b models, Model1 and Model2, are shown in Fig. 1. For each system, we ran three independent, 1-μs long, trajectories.

*Root-mean square deviation.* We assessed the protein structural stability in the paracellular cleft by calculating the time evolution of the RMSD of the pore-forming ECL domains. In Fig. 2a,b, we report the average RMSD values for all the ECL domains (upper panels) and the values for individual pores (lower panels). All profiles display a plateau, which is indicative of stable conformations. Model2 deviates more from the starting structure with respect to Model1, probably because of the use of additional restraints in the latter.

*Pore radius.* The pore radii of the paracellular channels were calculated using HOLE [80]. Fig. 2c,d show the radius along the channel axis (central pore) for the Cldn10b Model1 and Model2, compared with that of Cldn15 (Fig. S3a). All systems are characterized by the typical hourglass shape previously observed in JDR-based architectures [42,47,48]. For both Cldn10b models, the maximal pore constriction is about 2.2 Å, at the pore center, smaller than that found for the Cldn15 multi-pore architecture (Fig. 2c,d, purple dashed line).

*Assessment of the cis-linear interactions.* The simulation of multi-pore structures permits the analysis of the intermolecular *cis-linear* interactions that stabilize the TJ strand [14,40]. In the Cldn15 crystal structure (PDB ID: 4P79 [40]), this network is mainly established by the residue M68 of one monomer fitting the hydrophobic cage arranged by residues F146, F147, and L158 of the neighboring one. These amino acids are conserved among various Cldn homologs, including Cldn10b (Fig. S3b). The *cis-linear* interactions were monitored by calculating inter-residue distances for both Model1 (Fig. 3a,b) and Model2 (Fig. 3c, d), and compared to values for the same distances from the Cldn15 crystal (Fig. 3c,d, red dotted lines). Results are also summarized in Table 1. In Model1, d1 and d3 are stable and consistent with those in the Cldn15 crystal (d1 * and d3 *; Fig. 3b). The distance between M69 and F147 (d2) exhibits minimal fluctuations but differs by $\sim 2$ Å from the crystal one (d2 *). Similar results are found for Model2 (Fig. 3d), where

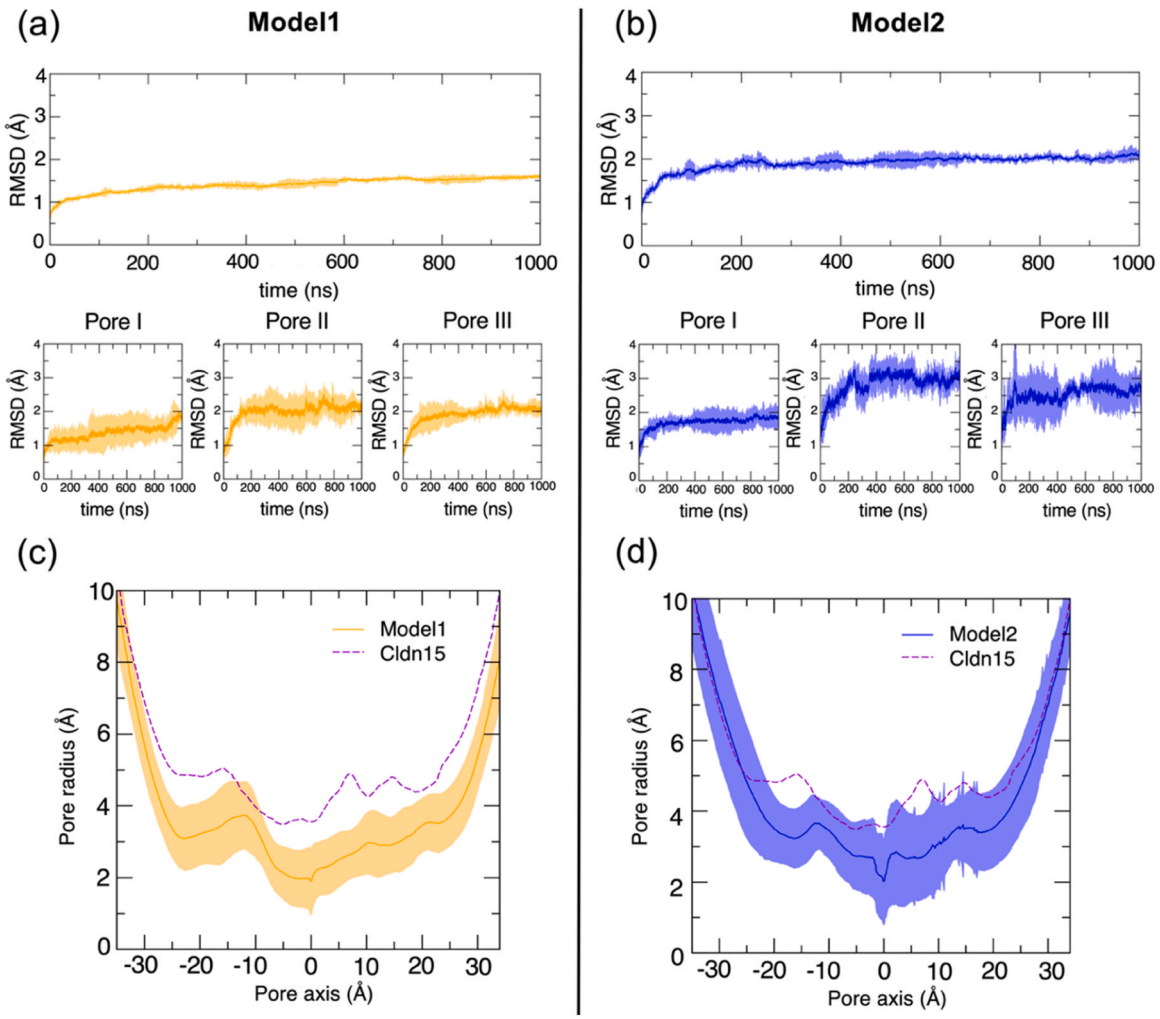


**Fig. 2.** Structural analysis of the Claudin-10b triple-pore models. (a,b) Backbone RMSD of the ECL domains of Model1 and Model2, respectively. Upper panels: all paracellular domains. Lower panels: individual pores. (c,d) Central pore radii of Model1 and Model2, respectively, compared to that of Cldn15 multi-pore (purple dotted line). Dark lines indicate the averages over each system's replica, while shaded areas represent the standard deviations.

all distances are stable, d1 is consistent with d1 * , but small differences (~ 1 Å) are observed between d2 and d3 and the corresponding crystal values (d2 * and d3 *).

*Analysis of the electrostatic paracellular space* . The distribution and orientation of the charged pore-lining residues govern the ion-selectivity of Cldn pores [92]. As noted before [50,51], in Cldn10b the paracellular cavities of both Model1 (Fig. 4a) and Model2 (Fig. 4b) are largely populated by acidic residues facing the lumen of each pore. In correspondence with the maximal constriction, four D56 residues form a ring and point their sidechains towards the lumen. Moving towards the exits of the channels, two couples of D36 and E153 residues are symmetrically oriented in the intermediate segments, while the D73 and E145 ones are located at the two entrances. On the other hand, the basic amino acids are located far from the pore volume, except for K64, pointing towards the lumen. As a result, the electrostatic surface of both paracellular models (Fig. 4b,d) exhibits a predominantly acidic character, more pronounced in Model2 than in Model1, especially in the regions close to the pairs formed by D36 and E153 . Only few basic areas are revealed, near the TM domains. On the contrary, no relevant hydrophobic regions are found inside these systems, so that water is unlikely to be blocked by a hydrophobic gating mechanism, contrary to what was previously suggested [32].

To highlight the differences in the position of the acidic pore-lining residues in the two models, we calculated distances between the side chains of each pair of residues facing across the cavities (d4 to d8). Representative snapshots of Model1 and Model2, highlighting the amino acids used to define the distances, are reported in Fig. 5a and c, whereas Fig. 5b and d show how all distances evolve over time. Major variations are found for d4 (~8 Å) and d7 (~17 Å) because of the dissimilar orientation of the $\beta1\beta2$ loops in the two Cldn10b models (Fig. S4). The orientation of the D36 pairs in the two models (Fig. 5a,c d7) correlates with the differences observed in the electrostatic surfaces (Fig. 4), since the displacement of the two acidic amino acids away from the pore lumen decreases the acidity of the paracellular cavity of Model1. Interestingly, at the constriction centers, the distances between D56 residues (d8) display only minor differences (~1 Å).

### 3.2. *Ion transport is mediated by pore-lining acidic sites*

After the assessment of the structural properties of the two models, we analyzed the details of $Na^+$ transport through the Cldn10b and Cldn15 pores. The path of $Na^+$ ions entering the central cavity of each system was monitored by tracking their position along the pore axis, corresponding to the Cartesian *y* coordinate. Results for one replica of Cldn10b Model1 and Model2 are reported in Fig. 6a and b, respectively, while other replicas are shown in Fig. S5. In these panels, each color represents the trajectory of a single $Na^+$ ion found within the pore, i.e., with a *y* coordinate between −30 Å and 30 Å. It can be observed that

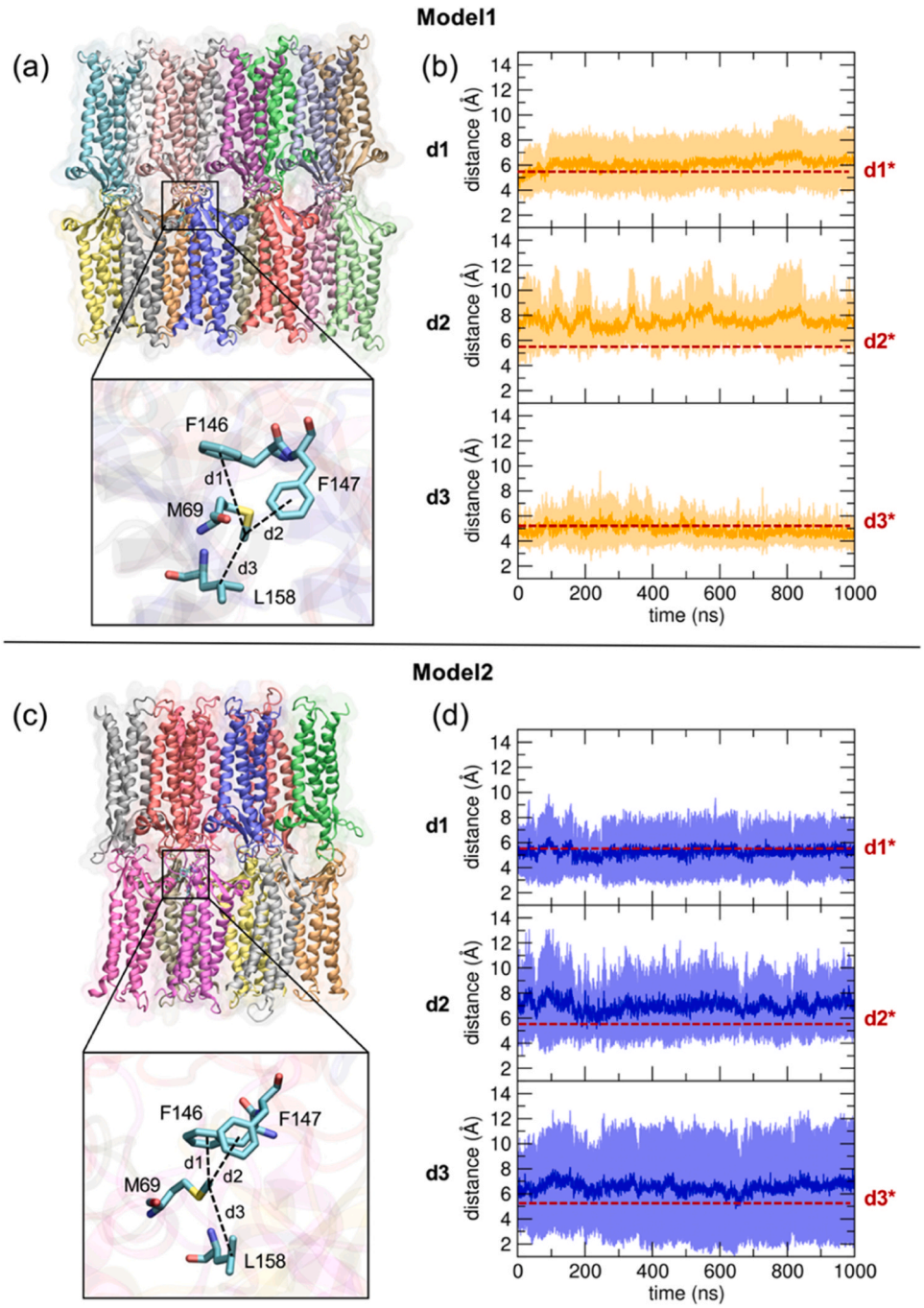


**Fig. 3.** Analysis of the cis-linear interactions in the Claudin-10b triple-pore models. (a,b) Representation and time evolution of the distances between M69 and F146 (d1), F147 (d2) and L158 (d3) for Cldn10b Model1 (central pore). (c,d) Same for Model2. Dark lines indicate the averages over each system's replica, while light areas represent the standard deviations. Red dotted lines are the corresponding values in the Cldn15 crystal structure (PDB ID: 4P79). Snapshots are taken from the starting configuration of each system.

most ions reside between −10 Å and + 10 Å along the pore axis in Model1 and between −15 Å and + 15 Å in Model2. In these channels, the acidic residues form coordination sites for ions that remain stably bound or interchange. Consistently, the distributions of $Na^+$ ion along the pore axis, calculated using all simulated replicas (Fig. 6c), show three peaks in both models, corresponding to the positions of the D56 residues, in the middle, and of D36 and E153 at the sides. The peaks corresponding to D36 and E153 are less pronounced in Model1 than in Model2, likely because of the more peripherical position of these residues in the former (see differences in distances d6 and d7 in Fig. 5). To evaluate the hydration state of the permeating ions, we calculated the average number of water molecules bound to each $Na^+$ ion inside the central cavity. Results indicate that the ions are coordinated by ~ 5 water molecules at the pore mouths of Model1 and Model2, where they interact with D73 and E145 (Fig. S4). On the other hand, the ions lose up to three water molecules when bound to the acidic residues within the pore (E153, D36, D56).

The average number of $Na^+$ ions occupying the paracellular cavities varies in the two structures: about 5 and 8 $Na^+$ ions are found inside Model1 and Model2 pores, respectively (Fig. 6d). Since both Cldn10b and Cldn15 are known to be cation-selective, we compared these results to those for Cldn15. Despite the latter's greater pore size, we found that

**Table 1**
Distances of the Claudin-10b triple pore models. Atom names between parentheses are indicated as follows: CD is the side chain Cδ atom, CE the Cε atom, and CG the Cγ atom, while COM is the center of mass of the aromatic side chain. For distances d1, d2 and d3, corresponding to the cis-linear interactions, the corresponding distances from the Cldn15 crystal structure (d1 *, d2 * and d3 * in Fig. 3) are reported (central pore).

| Distance name | Residues (atoms) | analysis | Distance (Å) | | |
|---|---|---|---|---|---|
| | | | Model1 | Model2 | Claudin-15 crystal (PDB ID: 4P79 [40]) |
| **d1** | M69 (CE) – F146 (COM) | *Cis-linear* interactions | 6.09 ± 0.41 | 5.26 ± 0.33 | 5.33 |
| **d2** | M69 (CE) – F147 (COM) | | 7.58 ± 0.47 | 6.99 ± 0.50 | 5.29 |
| **d3** | M69 (CE) – L158 (CG) | | 4.92 ± 0.40 | 6.53 ± 0.43 | 5.10 |
| **d4** | D73 (CG) – D73 (CG) | Acidic pore-lining residues cross-distances | 15.71 ± 0.48 | 23.85 ± 0.96 | |
| **d5** | E145 (CD) – E145 (CD) | | 21.68 ± 0.90 | 20.53 ± 0.49 | |
| **d6** | E153 (CD) – E153 (CD) | | 11.17 ± 1.38 | 12.94 ± 1.27 | |
| **d7** | D36 (CG) – D36 (CG) | | 28.71 ± 1.12 | 11.09 ± 0.48 | |
| **d8** | D56 (CG) – D56 (CG) | | 12.86 ± 0.50 | 11.31 ± 0.78 | |

the number of cations in its cavities is approximately the same as Cldn10b Model1 (~5 $Na^+$ ions). On the other hand, both Cldn10b models show a significantly lower rate of $Na^+$ ions fully traversing the pores - that is, entering from one side and escaping from the other - than Cldn15 (Fig. 6e).

### 3.3. *The water flux through Claudin-10b is slowed down compared to Claudin-15*

We then investigated water permeation through the Cldn10b channels, and compared it with that of Cldn15. Fig. 7a shows snapshots from simulations of the three systems, where it can be observed that the paracellular cavities are fully hydrated. However, relevant differences are found between the water fluxes through the two Cldns. First, compared to Cldn15, both Cldn10b models can fit fewer water molecules in the cavity (Fig. 7b). Secondly, the rate at which water molecules fully traverse the pore is substantially lower for Cldn10b (Fig. 7c). To check whether these water molecules belong to the cation hydration shells, we calculated the percentage of time spent by each of them as part of the coordination sphere of $Na^+$ ions within the pore.

Fig. 7d shows that, in the Cldn10b Model1, approximately 50 % of the permeating water molecules do not interact with $Na^+$ ions, while the remaining molecules bind $Na^+$ for a maximum of 5 % of the trajectory, and, in any case, for less than 20–30 %. For Model2 and Cldn15, about 20 % of the crossing waters are never part of the hydration shells; the remaining ones coordinate ions for less than 40 % of the time and up to about 10 % of the time at most.

Overall, the standard MD simulations suggest that, albeit to a different extent in the two models, $Na^+$ ions populating the Cldn10b pores strongly interact with the acidic pore-lining residues. The rate of translocating water molecules is also smaller than in Cldn15, and most of them traverse the pore as free diffusing molecules, being part of $Na^+$ hydration shells only for small portions of the trajectories.

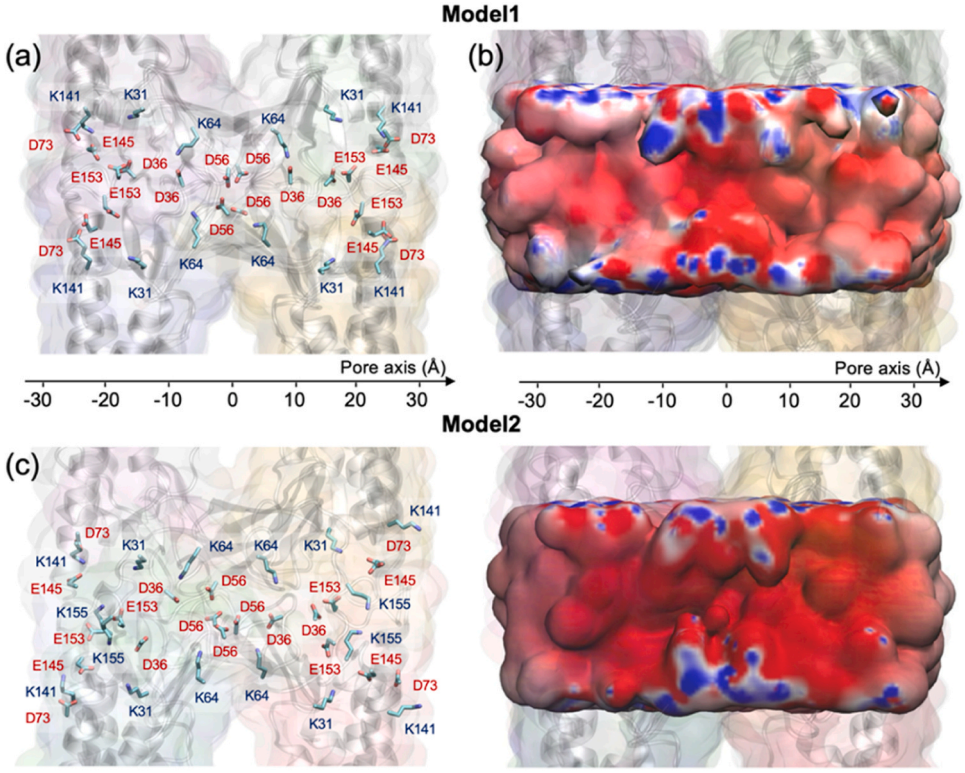


**Fig. 4.** Paracellular composition of the Claudin-10b triple-pore models. (a,b) Orientation of charged pore-lining residues and electrostatic surface in Model1; (c,d) same for Model2. The electrostatic surfaces are represented with a color-code ranging from red (−18 kT/e) to white to blue (+18 kT/e). The sections of the central pores of the two equilibrated systems are shown.

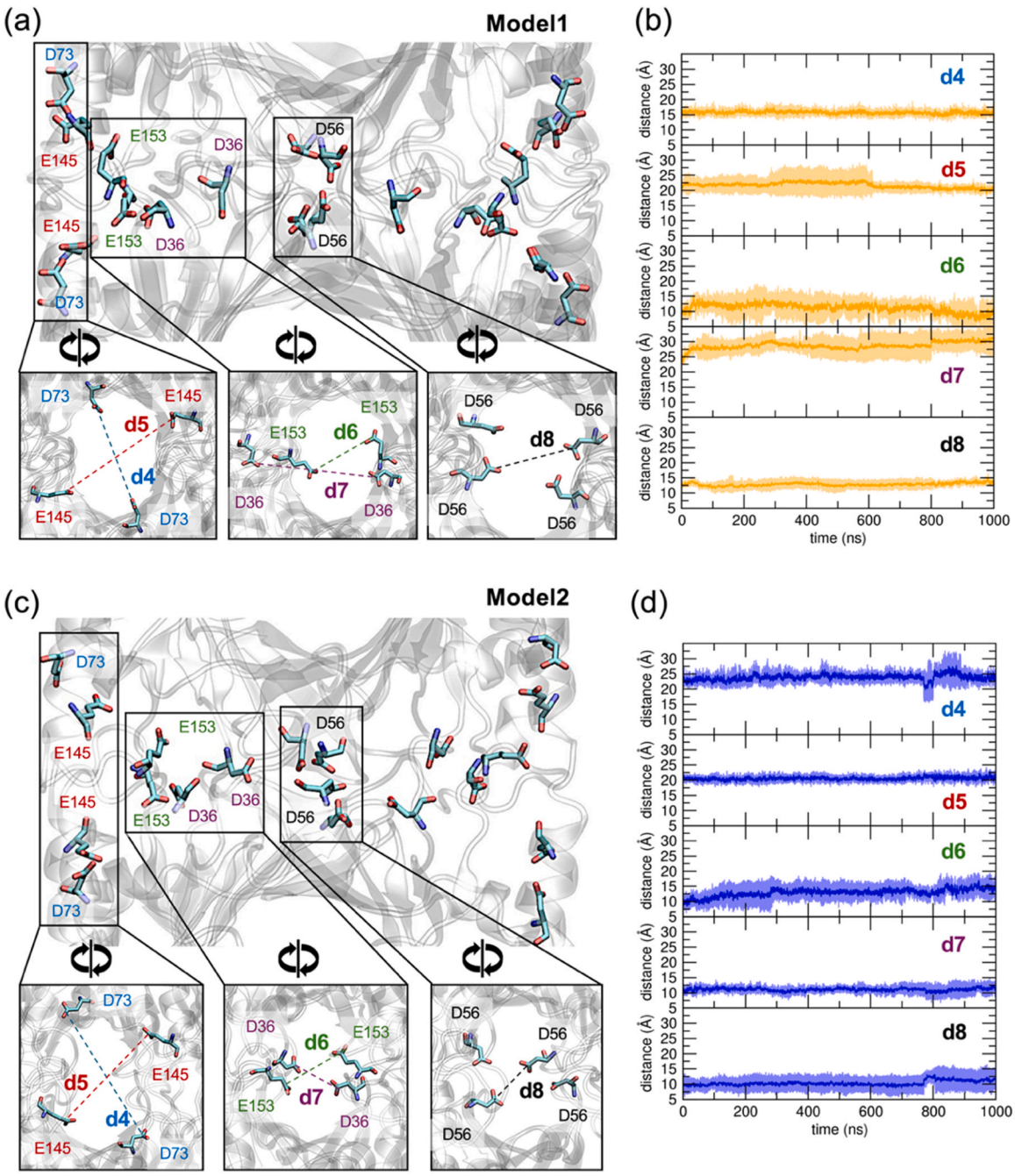


**Fig. 5.** Cross-distances between opposing acidic pore-lining residues. (a,b) Illustration and time-evolution of distances between facing acidic amino acids in Model1: d4 (D73-D73), d5 (E145-E145), d6 (E153-E153), d7 (D36-D36) and d8 (D56-D56); (c,d) same for Model2. Dark lines indicate the averages over all replicas and monomer pairs, while light areas represent the standard deviations. Snapshots represent the central pore at the end of the standard MD run for a representative simulation of each Cldn10b model.

We then monitored the extent to which water molecules establish direct interactions with pore-lining residues in Cldn10b and Cldn15. Indeed, the distribution of the polar, apolar and charged residues regulates water distribution and orientation on proteins surface and within hydrophilic cavities [93].

Fig. S7a shows that the paracellular domains of the two Cldn10b models and of the Cldn15 one are largely populated by polar amino acids (green regions), followed by apolar (grey regions), acidic (red regions) and basic (blue regions) residues. The number of water HBs formed by polar and apolar residues is approximately the same for Cldn10b and Cldn15 (Fig. S7b, Table S2). Most of the HBs formed by polar amino acids are found at the center of the cavity (Fig. S7B, green line), and, in each system, they are three times more frequent than those formed by apolar amino acids. On the other hand, the HBs formed by water and acidic residues are considerably more in the Cldn10b models compared to Cldn15 (Table S2), because of the larger number of such residues facing the lumen in Cldn10b (five and three per monomer in Cldn10b and Cldn15, respectively). The Cldn10b water-interacting residues D36, D73, and E153 are found at the pore entrances (Fig. S7b, red line), while in Cldn15 they are replaced by histidine, serine, and glycine (Fig. S3), which form only few. Also for basic residues we found more HBs with water in Cldn10b than in Cldn15, although there are few positively-charged residues in the pore of both systems (three and one per monomer in Cldn10b and Cldn15, respectively).

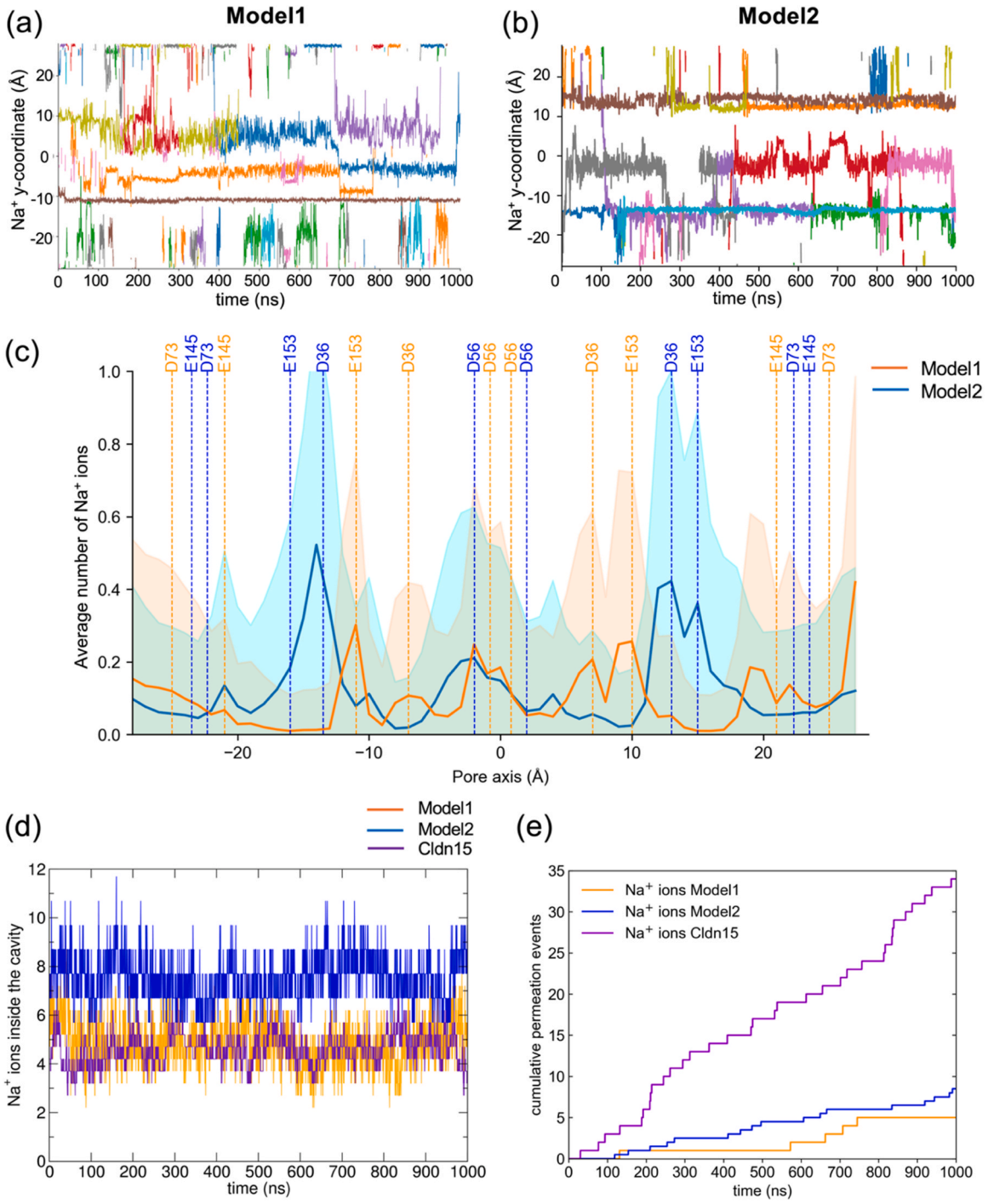


**Fig. 6.** Ion conduction through multi-pore architectures. (a,b) Time-evolution of $Na^+$ positions inside the central pore of Cldn10b Model1 and Model2, respectively. Each color corresponds to a different cation. Only ions that spent at least 10 % of the total time inside the pore are shown for clarity. (c) Distributions of $Na^+$ ions along the pore axis. The profiles and the associated errors are calculated as mean and standard deviation over the three replicas of each model. Dashed lines correspond to the positions of C$\alpha$ atoms in the equilibrated structures. (d) Number of $Na^+$ ions inside the pores along the simulated trajectories (averaged over the replicas for Cldn10b). (e) Cumulative number of ions that crossed Cldn10b Model1 (orange), Model2 (blue), or Cldn15 (purple) pore during the MD simulations. Traversing in both directions was considered and data for Cldn10b were averaged over replicas.

### *3.4. Free energy calculations of ion and water permeations*

To quantify the selectivity properties of Cldn10b paracellular architectures, we calculated the one-dimensional FE profiles for single ions or water molecules permeating through the pores, using the US-WHAM method [83,94]. In the calculations, all ions except the tagged one were kept outside the pore. Results show that in both Model1 (Fig. 8a) and Model2 (Fig. 8b) the passage of the anion is hindered by FE barriers of ~11 kcal/mol, peaked at the center of the pore, in correspondence with the maximal constriction and the ring of negatively charged D56 residues. Consistently, the profiles for $Na^+$ and $K^+$ show deep attractive minima in the same region. However, the $Cl^-$ curves of the two models have different shapes, whereas those of the cations differ in profile and minimum depth. While, in Model1, the barrier to the anion is narrower, growing beyond 10 kcal/mol only between −10 Å and 10 Å, in Model2 it is much broader. The cation profiles have the same difference in

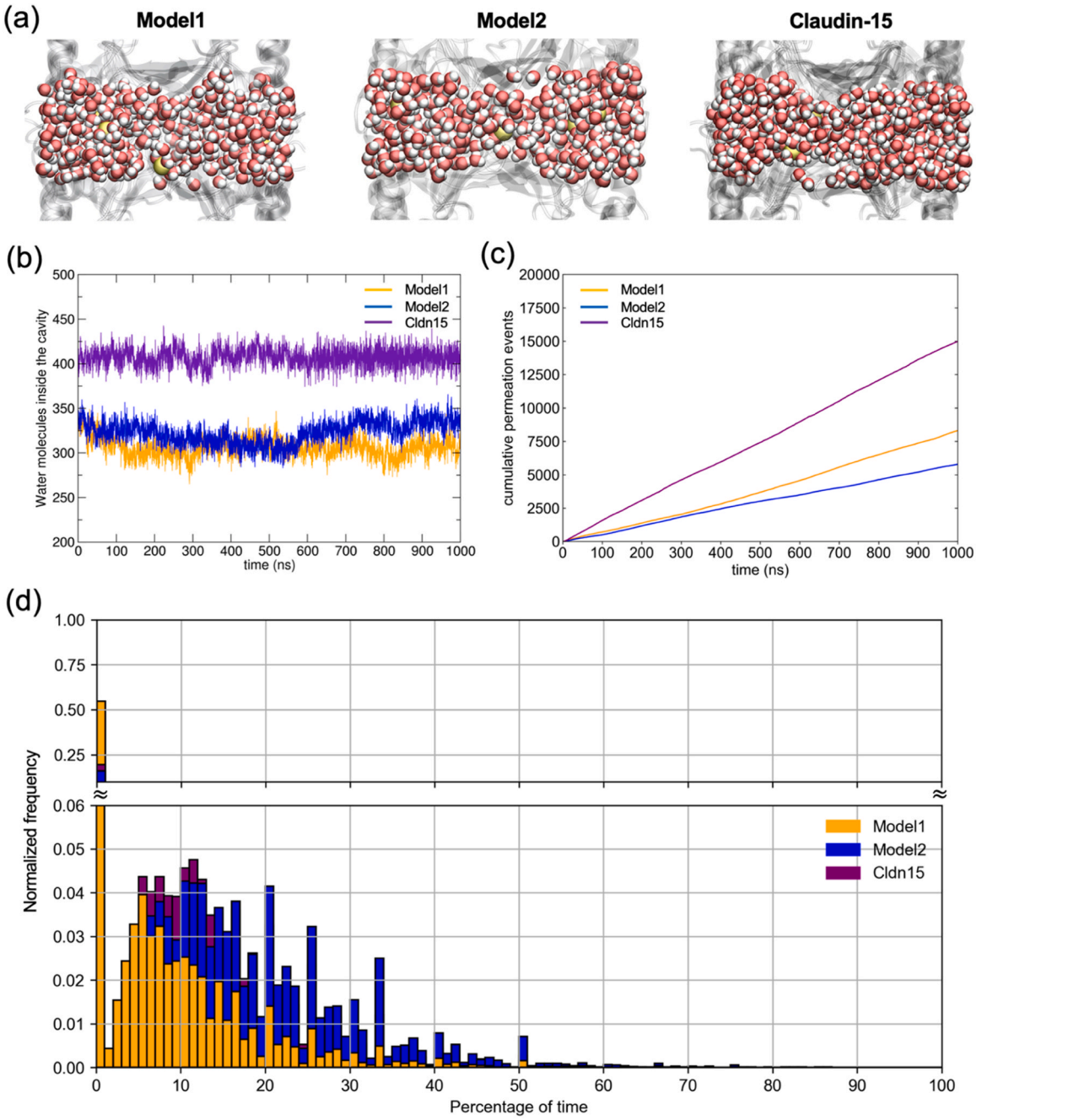


**Fig. 7.** Water permeation through the Claudin-10b and Claudin-15 models. (a) Representative snapshots of the hydrated central paracellular cavities of Cldn10b and Cldn15 models taken after 100 ns of standard MD simulation. (b) Average number of water molecules inside Cldn10b Model1 (orange), Model2 (blue) and Cldn15 (purple) pores. (c) Cumulative number of water molecules that progressively crossed the Cldn10b Model1 (orange), Model2 (blue) or Cldn15 (purple) pores. Traversal in both directions was considered, and data for Cldn10b were averaged over replicas. (d) Histograms reporting the percentage of time each water molecule is coordinated to a $Na^+$ ion while traversing the pore.

width, but while the minima reach about −5 kcal/mol in Model1, they are −9 kcal/mol in Model2. These differences arise from the positions and orientation of the pairs formed by the D36 and E153 residues in the two models. Indeed, in Model2 they are positioned farther away from the middle of the pore axis. Moreover, the D36 residues in Model2 are closer to the pore lumen and with their side chains oriented towards it (see Fig. 5). These findings are consistent with those from standard MD simulations, which indicated that Model1 pore is less populated by $Na^+$ ions than Model2 (Fig. 6d). Finally, the FE profiles for the permeation of a single water molecule indicate a barrierless process in both models (Fig. 8a and b, black line). Although not completely unexpected, given the full hydration of cavities seen in standard MD (Fig. 7a,b), this result seems not to agree with the limited water permeation observed in the Cldn10b models (Fig. 7c). Opposite to standard MD, however, the FE calculations were performed with no ions inside the pores, and so we set out to determine whether the profiles would change if we allowed $Na^+$ ions within the cavity.

We then repeated the US calculations for water permeation through the pores by considering different conformations of bound ions, based on configurations observed in the standard MD trajectories. We started with one $Na^+$ ion in Model1, at the central D56 ring (Fig. S8a), and three $Na^+$ ions in Model2, one coordinated by the central D56 residues and two by the pairs of D36 (Fig. S8b). Results show again no barriers to water permeation in both models with limited ion occupation (Fig. S8c).

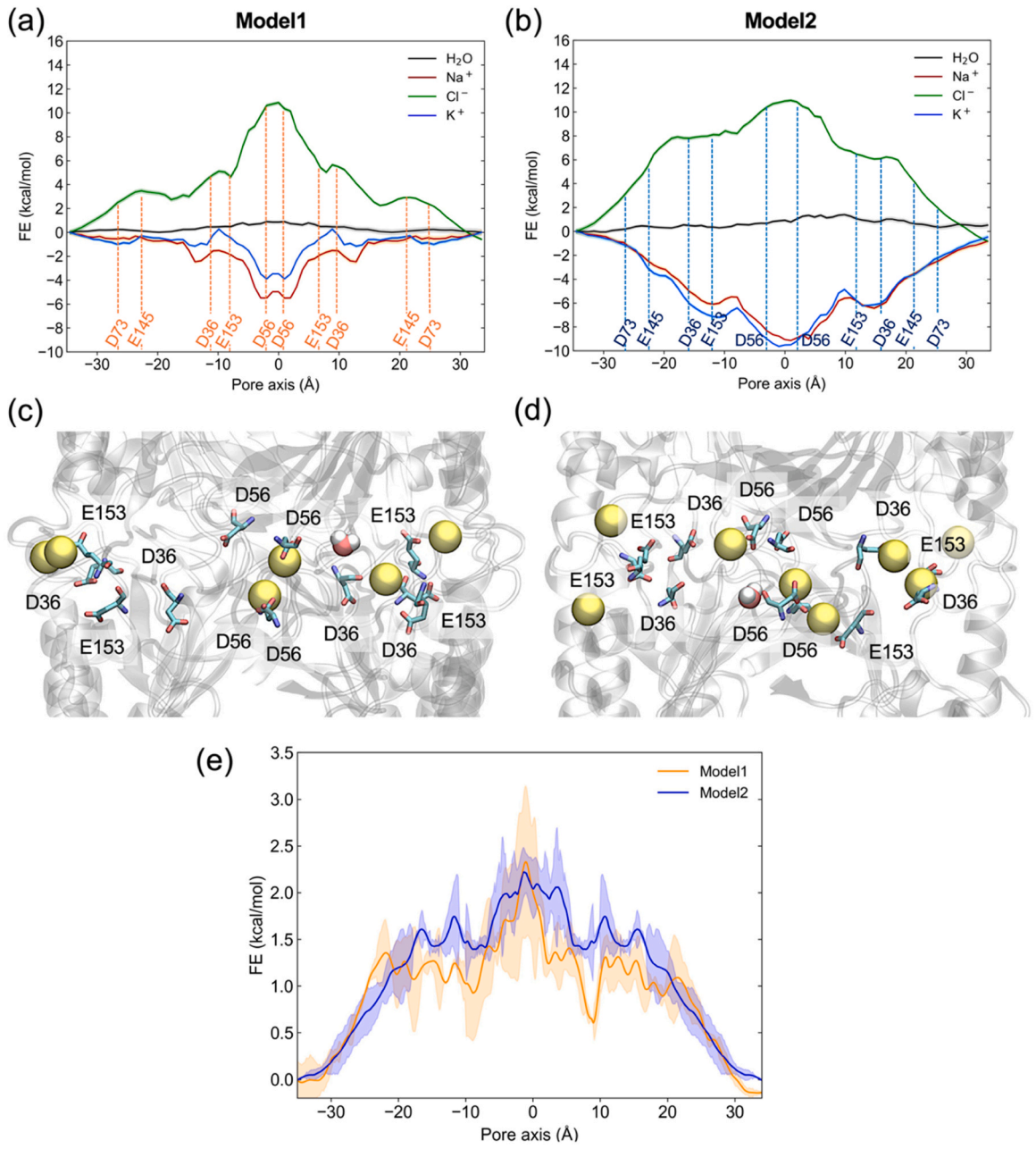


**Fig. 8.** Free energy calculations of ions and water permeation through the Claudin-10b pores. (a,b) FE profiles of single-ion/water molecules permeation through Model1 and Model2 central pores, respectively. The positions of pore-lining acidic residues, identified by the coordinates of their Cα atoms in the equilibrated structure, are indicated. (c,d) Representative snapshots of Model1 and Model2 configurations selected to compute the FE profiles of water permeation in the presence of multiple $Na^+$ ions inside the pore. (e) FE profiles of water permeation through ion-occupied Model1 and Model2 central pores.

We then increased the number of $Na^+$ atoms inside the pores, using configurations representative of the $Na^+$ average occupancy observed during the unbiased trajectories, i.e., six $Na^+$ ions in Model1 (Fig. 8c) and eight $Na^+$ ions in Model2 (Fig. 8d). The cations were confined within the pores but left free to move inside of them. These additional calculations were performed using TAMD [89], and resulted in symmetrical FE profiles with maxima of ~ 2.2 kcal/mol for both Model1 and Model2, localized at the center of the pore (Fig. 8e). These results indicate that the higher the number of $Na^+$ ions inside the pore, the more limited is the passage of water, thus suggesting that the restricted permeability of Cldn10b to water is due to a blockade caused by cations within the cavity.

## 4. Discussion

The recent endeavors to elucidate the structural organization of Cldn proteins within epithelial and endothelial TJ strands have profited from using computational methods to address both their functional [42–44, 46–51,53,84] and mechanical [45,95,96] features. Most of these investigations employed the structural template introduced by Suzuki et al., [39] based on the Cldn15 crystal [40]. This *joined-double row* (JDR) model has been successfully validated for many homologs with different physiological functions, including Cldn2 [46], Cldn4 [48], Cldn5 [47,84], Cldn10a [50], Cldn10b [50], and Cldn15 [42–44]. In all these works, it has been shown that the electrostatic environment produced by the pore-lining residues governs the accessibility of the ions. However, little attention has been devoted to the transport of water. The

mechanistic description of this phenomenon represents a notable challenge. Indeed, while the size of water molecules (VdW radius ~ 1.7 Å [97]) allows the passage through the pores, some Cldn subspecies are permeable to ions but not to water. Cldn10b is a remarkable example, as it is expressed in the thick ascending limb of the nephron's loop of Henle, where it forms channels permeable to cations but not to water [32,37].

In this work, we used MD simulations to test whether two variants of the JDR structural model for paracellular TJs can recapitulate the selectivity properties of Cldn10b. Both variants comprise three pores and represent a realistic proxy of the multimeric organization of Cldn proteins in TJs, including interactions stabilizing the aggregates within the same cell and across the paracellular cleft. However, they differ in the orientation of the segment connecting the $\beta$1 and $\beta$2 strands of each monomer's ECL1 (the $\beta1\beta2$ loop), which was missing from the original JDR architecture and had to be modeled. Since different loop conformations result in distinct orientations of residues that are known to be relevant for Cldn selectivity, it was questioned whether both models could reproduce the functional properties of paracellular channels.

Our MD simulations on the microsecond timescale indicate that the two conformations are stable and have a comparable pore shape and size, with a minimal radius of about 2.2 Å at the center, consistent with the values reported by Nagarajan et al. [50,51]. This is smaller than those found in all multi-pore systems modeled so far for channel-forming Cldns, such as Cldn2 [46,52,98] (minimal radius ~ 3.4 Å), Cldn4 [48,52] (~ 3.2 Å), and Cldn15 [43,52,99] (~3.8 Å), suggesting that the steric factor plays a critical role in the regulation of paracellular transport. In particular, the difference with Cldn15 is in line with previous computational [39,43,44,51] and experimental data [19,35,36,49].

Both models show multiple $Na^+$ binding sites within the pores (corresponding to residues D56, D36, and E153), among which ions can exchange while shedding part of their hydration shell. The D56 ring, previously identified as the selectivity filter [37,49], is located at the central and narrowest region of the pore. The only basic residue lining the pore axis is K64 that, as previously suggested [51], may compete with cations for interactions with acidic residues, establishing transient contacts with the neighboring D36 or D56. The cation-selective property of Cldn10b was reproduced for both architectures using single-ion FE calculations. Although the actual transport mechanism results from the crossing of multiple ions, the single-ion FE captures the fundamental features of ion-protein interaction as, for example, the location of binding sites and repulsive barriers. Our data show that both models generate FE barriers to the passage of anions while being attractive for cations. However, while the distinct $\beta1\beta2$ loop conformations do not affect the height of the barriers, they yield in different shapes and minima depths. In the structure from Piontek and collaborators (Model2), the curves are broader, and the minima are almost twice as deep as in Model1. This is due to the D36 residues that are closer to the pore axis, with their side chains pointing towards the lumen. The higher attractivity of Model2 for cations results in about 8 $Na^+$ ions found inside the pore, whereas in Model1 and Cldn15 they are around 5. This notwithstanding, the flux of cations across both Cldn10b structures is much smaller than in Cldn15, probably due to the largest pore size of Cldn15 which avoids jamming of ions. Finally, water permeation analysis reveals that Cldn10b channels can accommodate approximately 20 % fewer water molecules than the wider Cldn15 ones, with a flux across the pore that is 2–3 times smaller. The mechanism of water crossing, however, is different between the two Cldn10b models, with more free molecules traversing the pore in Model1 than in Model2. This might be a consequence of the smaller number of ions inside Model1 pore, resulting in fewer interactions with water.

Altogether, our data demonstrate that both Cldn10b pore models are cation-selective, albeit to a different extent, and that they are less permeable to both $Na^+$ and water compared to Cldn15, qualitatively consistent with the experimental evidence [32,35,37]. Indeed, Rosenthal et al. estimated absolute permeabilities to $Na^+$ of $\sim 14 \times 10^{-6}$ cm • $s^{-1}$ for Cldn15 in MDCK C7 cells, and observed the formation of water flux under osmotic gradient [35]. On the other hand, $Na^+$ permeability of $\sim 6.5 \times 10^{-6}$ cm • $s^{-1}$ and no water flux were found for Cldn10b overexpressed within the same cell line [36]. This behavior might result from the combination of the strongly acidic character and the narrow size of the Cldn10b pores. These characteristics cause jamming of cations within the cavity and the formation of HBs between water molecules and the pore-lining residues, that restrict the passage of the solvent across the pore. Such a mechanism confirms some previous hypotheses [51] and is supported by our FE calculations, which showed increased FE barriers for water when $Na^+$ ions crowd the pore.

The differential selectivity for ions and water represents a challenge for computational and experimental investigations. To date, theoretical studies have mostly been devoted to canonical transmembrane channels [100–109]. Some works [110–113] showed that, in narrow pores, apolar residues might create dry regions that could stop the flow of water and ions even without mechanical closure of the pathway (hydrophobic gating). A similar mechanism was originally supposed for Cldn10b,[32] but the hydrophilic environment of the pore and the flat FE profiles obtained for single-water molecule calculations do not support this hypothesis.

In summary, our data show that the JDR model, even with different conformations of the ECLs, is compatible with Cldn channels that are selective for ions and not for water.

This study offers insights into the molecular mechanism underpinning paracellular water selectivity, a crucial component of epithelial transport systems. However, the small FE barriers and the large number of solvent molecules found in the paracellular space do not fully agree with null water transport through the Cldn10b pores. Thus, although the observed water and Na+ permeabilities are qualitatively in agreement with experimental data [32,35,37], the water/Na+ ratio obtained for the Cldn10b models is at least comparable or even higher than Cldn15. This discrepancy might be due to known limitations of the MD technique that hamper quantitative agreement between computational studies of ion permeation and experiments, such as the short time-length of the trajectories, or possible flaws in the representations of atomic interactions [114]. In particular, the CHARMM force field does not treat explicitly electronic polarization effects. In addition, in our simulations we do not consider ion or water concentration gradients between the two sides of the paracellular pore. Future investigations shall benefit from the simulations of larger Cldn complexes for longer times and with more accurate force fields, in order to account for the experimental findings that are not yet captured.

## Ethic statements

In this work, no animal or human study is presented.

## Funding

The research was supported by IRCCS Ospedale Policlinico San Martino (Ricerca Corrente and 5 × 1000 grants to FB and LM), the Italian Ministry of Health (GR-2021-12372966 grant to FB) and by Telethon/Glut-1 Onlus Foundations (GSP19002_PAsGlut009 and GSA22A002 projects to FB). Open Access Funding were provided by Università Politecnica delle Marche within the CRUI-CARE Agreement.

## CRediT authorship contribution statement

**Alessandro Berselli:** Writing – review & editing, Writing – original draft, Visualization, Investigation, Formal analysis, Data curation, Conceptualization. **Giulio Alberini:** Writing – review & editing, Supervision, Project administration, Investigation, Formal analysis, Conceptualization. **Fabio Benfenati:** Writing – review & editing, Supervision, Funding acquisition. **Luca Maragliano:** Writing – review & editing, Supervision, Project administration, Investigation, Funding acquisition, Formal analysis, Conceptualization.

## Declaration of Competing Interest

The authors declare that they have no known competing financial interests or personal relationships that could have appeared to influence the work reported in this paper.

## Acknowledgments

We are grateful to Dr. Jörg Piontek and Dr. Santhosh Kumar Nagarajan for providing their Cldn10b triple-pore model, here named Model2, for a careful reading of the manuscript and for many fruitful discussions. We also thank Profs. Michael Fromm and Dorothee Günzel, and Dr. Rita Rosenthal for useful suggestions. We acknowledge the HPC infrastructure and the Support Team at Fondazione Istituto Italiano di Tecnologia. In particular, we thank Alessia Vignolo, Sergio Decherchi and Mattia Pini for their kind assistance. We also thank Diego Moruzzo, Ilaria Dallorto, Rossana Ciancio and Arta Mehilli for administrative assistance and technical help. We acknowledge CINECA awards under the ISCRA initiative, for the availability of high-performance computing resources and support.

## Appendix A. Supporting information

Supplementary data associated with this article can be found in the online version at doi:10.1016/j.csbj.2024.11.025.

## References

[1] Boado RJ, Li JY, Nagaya M, Zhang C, Pardridge WM. Selective expression of the large neutral amino acid transporter at the blood-brain barrier. Proc Natl Acad Sci USA 1999;96:12079–84. https://doi.org/10.1073/pnas.96.21.12079.
[2] Cornford EM, Hyman S, Swartz BE. The human brain GLUT1 glucose transporter: ultrastructural localization to the blood-brain barrier endothelia. J Cereb Blood Flow Metab 1994;14:106–12. https://doi.org/10.1038/jcbfm.1994.15.
[3] Kido Y, Tamai I, Okamoto M, Suzuki F, Tsuji A. Functional clarification of MCT1-mediated transport of monocarboxylic acids at the blood-brain barrier using in vitro cultured cells and in vivo BUI studies. Pharm Res 2000;17:55–62. https://doi.org/10.1023/a:1007518525161.
[4] Nguyen LN, Ma D, Shui G, Wong P, Cazenave-Gassiot A, Zhang X, et al. Mfsd2a is a transporter for the essential omega-3 fatty acid docosahexaenoic acid. Nature 2014;509:503–6. https://doi.org/10.1038/nature13241.
[5] Farquhar MG, Palade GE. Junctional complexes in various epithelia. J Cell Biol 1963;17:375–412.
[6] Gonschior H, Schmied C, Van der Veen RE, Eichhorst J, Himmerkus N, Piontek J, et al. Nanoscale segregation of channel and barrier claudins enables paracellular ion flux. Nat Commun 2022;13:4985. https://doi.org/10.1038/s41467-022-32533-4.
[7] Anderson JM. Molecular structure of tight junctions and their role in epithelial transport. Physiology 2001;16:126–30. https://doi.org/10.1152/physiologyonline.2001.16.3.126.
[8] Colegio OR, Van Itallie CM, McCrea HJ, Rahner C, Anderson JM. Claudins create charge-selective channels in the paracellular pathway between epithelial cells. Am J Physiol Cell Physiol 2002;283:C142–7. https://doi.org/10.1152/ajpcell.00038.2002.
[9] Angelow S, Ahlstrom R, Yu ASL. Biology of claudins. Am J Physiol Ren Physiol 2008;295:F867–76. https://doi.org/10.1152/ajprenal.90264.2008.
[10] Günzel D, Yu ASL. Claudins and the modulation of tight junction permeability. Physiol Rev 2013;93:525–69. https://doi.org/10.1152/physrev.00019.2012.
[11] Berselli A, Benfenati F, Maragliano L, Alberini G. Multiscale modelling of claudin-based assemblies: a magnifying glass for novel structures of biological interfaces. Comput Struct Biotechnol J 2022;20:5984–6010. https://doi.org/10.1016/j.csbj.2022.10.038.
[12] Krause G, Winkler L, Mueller SL, Haseloff RF, Piontek J, Blasig IE. Structure and function of claudins. Biochim Biophys Acta Biomembr 2008;1778:631–45. https://doi.org/10.1016/j.bbamem.2007.10.018.
[13] Van Itallie CM, Anderson JM. Architecture of tight junctions and principles of molecular composition. Semin Cell Dev Biol 2014;36:157–65. https://doi.org/10.1016/j.semcdb.2014.08.011.
[14] Piontek J, Krug SM, Protze J, Krause G, Fromm M. Molecular architecture and assembly of the tight junction backbone. Biochim Biophys Acta Biomembr 2020;1862:183279. https://doi.org/10.1016/j.bbamem.2020.183279.
[15] Angelow S, Yu ASL. Structure-function studies of claudin extracellular domains by cysteine-scanning mutagenesis. J Biol Chem 2009;284:29205–17. https://doi.org/10.1074/jbc.M109.043752.
[16] Krause G, Winkler L, Piehl C, Blasig I, Piontek J, Müller SL. Structure and function of extracellular claudin domains. Ann N Y Acad Sci 2009;1165:34–43. https://doi.org/10.1111/j.1749-6632.2009.04057.x.
[17] Günzel D, Fromm M. Claudins and other tight junction proteins. Compr Physiol 2012;2:1819–52. https://doi.org/10.1002/cphy.c110045.
[18] Amasheh S, Meiri N, Gitter AH, Schöneberg T, Mankertz J, Schulzke JD, et al. Claudin-2 expression induces cation-selective channels in tight junctions of epithelial cells. J Cell Sci 2002;115:4969–76. https://doi.org/10.1242/jcs.00165.
[19] Günzel D, Stuiver M, Kausalya PJ, Haisch L, Krug SM, Rosenthal R, et al. Claudin-10 exists in six alternatively spliced isoforms that exhibit distinct localization and function. J Cell Sci 2009;122:1507–17. https://doi.org/10.1242/jcs.040113.
[20] Van Itallie CM, Rogan S, Yu A, Vidal LS, Holmes J, Anderson JM. Two splice variants of claudin-10 in the kidney create paracellular pores with different ion selectivities. Am J Physiol Ren Physiol 2006;291:F1288–99. https://doi.org/10.1152/ajprenal.00138.2006.
[21] Tamura A, Hayashi H, Imasato M, Yamazaki Y, Hagiwara A, Wada M, et al. Loss of claudin-15, but not claudin-2, causes Na+ deficiency and glucose malabsorption in mouse small intestine. Gastroenterology 2011;140:913–23. https://doi.org/10.1053/j.gastro.2010.08.006.
[22] Hou J, Goodenough DA. Claudin-16 and claudin-19 function in the thick ascending limb. Curr Opin Nephrol Hypertens 2010;19:483. https://doi.org/10.1097/MNH.0b013e32833b7125.
[23] Hou J, Renigunta A, Konrad M, Gomes AS, Schneeberger EE, Paul DL, et al. Claudin-16 and claudin-19 interact and form a cation-selective tight junction complex. J Clin Invest 2008;118:619–28. https://doi.org/10.1172/JCI33970.
[24] Tanaka H, Yamamoto Y, Kashihara H, Yamazaki Y, Tani K, Fujiyoshi Y, et al. Claudin-21 has a paracellular channel role at tight junctions. Mol Cell Biol 2016;36:954–64. https://doi.org/10.1128/MCB.00758-15.
[25] Breiderhoff T, Himmerkus N, Meoli L, Fromm A, Sewerin S, Kriuchkova N, et al. Claudin-10a deficiency shifts proximal tubular Cl- permeability to cation selectivity via claudin-2 redistribution. ASN.2021030286 J Am Soc Nephrol 2022. https://doi.org/10.1681/ASN.2021030286.
[26] Krug SM, Günzel D, Conrad MP, Rosenthal R, Fromm A, Amasheh S, et al. Claudin-17 forms tight junction channels with distinct anion selectivity. Cell Mol Life Sci 2012;69:2765–78. https://doi.org/10.1007/s00018-012-0949-x.
[27] Furuse M, Hata M, Furuse K, Yoshida Y, Haratake A, Sugitani Y, et al. Claudin-based tight junctions are crucial for the mammalian epidermal barrier: a lesson from claudin-1-deficient mice. J Cell Biol 2002;156:1099–111. https://doi.org/10.1083/jcb.200110122.
[28] Milatz S, Krug SM, Rosenthal R, Günzel D, Müller D, Schulzke J-D, et al. Claudin-3 acts as a sealing component of the tight junction for ions of either charge and uncharged solutes. Biochim Biophys Acta 2010;1798:2048–57. https://doi.org/10.1016/j.bbamem.2010.07.014.
[29] Nitta T, Hata M, Gotoh S, Seo Y, Sasaki H, Hashimoto N, et al. Size-selective loosening of the blood-brain barrier in claudin-5-deficient mice. J Cell Biol 2003;161:653–60. https://doi.org/10.1083/jcb.200302070.
[30] Denninger AR, Breglio A, Maheras KJ, LeDuc G, Cristiglio V, Demé B, et al. Claudin-11 tight junctions in myelin are a barrier to diffusion and lack strong adhesive properties. Biophys J 2015;109:1387–97. https://doi.org/10.1016/j.bpj.2015.08.012.
[31] Ben-Yosef T, Belyantseva IA, Saunders TL, Hughes ED, Kawamoto K, Van Itallie CM, et al. Claudin 14 knockout mice, a model for autosomal recessive deafness DFNB29, are deaf due to cochlear hair cell degeneration. Hum Mol Genet 2003;12:2049–61. https://doi.org/10.1093/hmg/ddg210.
[32] Rosenthal R, Günzel D, Theune D, Czichos C, Schulzke J-D, Fromm M. Water channels and barriers formed by claudins. Ann N Y Acad Sci 2017;1397:100–9. https://doi.org/10.1111/nyas.13383.
[33] Schnermann J, Huang Y, Mizel D. Fluid reabsorption in proximal convoluted tubules of mice with gene deletions of claudin-2 and/or aquaporin1. Am J Physiol-Ren Physiol 2013;305:F1352–64. https://doi.org/10.1152/ajprenal.00342.2013.
[34] Wilmes A, Aschauer L, Limonciel A, Pfaller W, Jennings P. Evidence for a role of claudin 2 as a proximal tubular stress responsive paracellular water channel. Toxicol Appl Pharmacol 2014;279:163–72. https://doi.org/10.1016/j.taap.2014.05.013.
[35] Rosenthal R, Günzel D, Piontek J, Krug SM, Ayala-Torres C, Hempel C, et al. Claudin-15 forms a water channel through the tight junction with distinct function compared to claudin-2. Acta Physiol (Oxf) 2020;228:e13334. https://doi.org/10.1111/apha.13334.
[36] Rosenthal R, Milatz S, Krug SM, Oelrich B, Schulzke J-D, Amasheh S, et al. Claudin-2, a component of the tight junction, forms a paracellular water channel. J Cell Sci 2010;123:1913–21. https://doi.org/10.1242/jcs.060665.
[37] Milatz S, Breiderhoff T. One gene, two paracellular ion channels-claudin-10 in the kidney. Pflug Arch 2017;469:115–21. https://doi.org/10.1007/s00424-016-1921-7.
[38] Citi S, Fromm M, Furuse M, González-Mariscal L, Nusrat A, Tsukita S, et al. A short guide to the tight junction. J Cell Sci 2024;137:jcs261776. https://doi.org/10.1242/jcs.261776.
[39] Suzuki H, Tani K, Tamura A, Tsukita S, Fujiyoshi Y. Model for the architecture of claudin-based paracellular ion channels through tight junctions. J Mol Biol 2015;427:291–7. https://doi.org/10.1016/j.jmb.2014.10.020.
[40] Suzuki H, Nishizawa T, Tani K, Yamazaki Y, Tamura A, Ishitani R, et al. Crystal structure of a claudin provides insight into the architecture of tight junctions. Science 2014;344:304–7. https://doi.org/10.1126/science.1248571.
[41] Krause G, Protze J, Piontek J. Assembly and function of claudins: structure-function relationships based on homology models and crystal structures. Semin Cell Dev Biol 2015;42:3–12. https://doi.org/10.1016/j.semcdb.2015.04.010.

[42] Alberini G, Benfenati F, Maragliano L. Molecular dynamics simulations of ion selectivity in a claudin-15 paracellular channel. J Phys Chem B 2018;122:10783–92. https://doi.org/10.1021/acs.jpcb.8b06484.

[43] Alberini G, Benfenati F, Maragliano L. A refined model of claudin-15 tight junction paracellular architecture by molecular dynamics simulations. PLOS ONE 2017;12:e0184190. https://doi.org/10.1371/journal.pone.0184190.

[44] Samanta P, Wang Y, Fuladi S, Zou J, Li Y, Shen L, et al. Molecular determination of claudin-15 organization and channel selectivity. J Gen Physiol 2018;150:949–68. https://doi.org/10.1085/jgp.201711868.

[45] Zhao J, Krystofiak ES, Ballesteros A, Cui R, Van Itallie CM, Anderson JM, et al. Multiple claudin-claudin cis interfaces are required for tight junction strand formation and inherent flexibility. Commun Biol 2018;1:50. https://doi.org/10.1038/s42003-018-0051-5.

[46] Irudayanathan FJ, Nangia S. Paracellular gatekeeping: what does it take for an ion to pass through a tight junction pore? Langmuir 2020;36:6757–64. https://doi.org/10.1021/acs.langmuir.0c00877.

[47] Berselli A, Alberini G, Benfenati F, Maragliano L. Computational assessment of different structural models for claudin-5 complexes in blood–brain barrier tight junctions. ACS Chem Neurosci 2022;13:2140–53. https://doi.org/10.1021/acschemneuro.2c00139.

[48] Berselli A, Alberini G, Benfenati F, Maragliano L. Computational study of ion permeation through claudin-4 paracellular channels. Ann NY Acad Sci 2022;1516:162–74. https://doi.org/10.1111/nyas.14856.

[49] Hempel C, Rosenthal R, Fromm A, Krug SM, Fromm M, Günzel D, et al. Tight junction channels claudin-10b and claudin-15: functional mapping of pore-lining residues. Ann N Y Acad Sci 2022;1515:129–42. https://doi.org/10.1111/nyas.14794.

[50] Nagarajan SK, Piontek J. Molecular dynamics simulations of claudin-10a and -10b ion channels: with similar architecture, different pore linings determine the opposite charge selectivity. Int J Mol Sci 2024;25:3161. https://doi.org/10.3390/ijms25063161.

[51] Nagarajan SK, Klein S, Fadakar BS, Piontek J. Claudin-10b cation channels in tight junction strands: octameric-interlocked pore barrels constitute paracellular channels with low water permeability. Comput Struct Biotechnol J 2023;21:1711–27. https://doi.org/10.1016/j.csbj.2023.02.009.

[52] Irudayanathan FJ, Wang X, Wang N, Willsey SR, Seddon IA, Nangia S. Self-assembly simulations of classic claudins-insights into the pore structure, selectivity, and higher order complexes. J Phys Chem B 2018;122:7463–74. https://doi.org/10.1021/acs.jpcb.8b03842.

[53] Irudayanathan FJ, Wang N, Wang X, Nangia S. Architecture of the paracellular channels formed by claudins of the blood-brain barrier tight junctions. Ann N Y Acad Sci 2017;1405:131–46. https://doi.org/10.1111/nyas.13378.

[54] Waterhouse A, Bertoni M, Bienert S, Studer G, Tauriello G, Gumienny R, et al. Swiss-model: homology modelling of protein structures and complexes. W296–303 Nucleic Acids Res 2018;46. https://doi.org/10.1093/nar/gky427.

[55] Heo L, Lee H, Seok C. GalaxyRefineComplex: refinement of protein-protein complex model structures driven by interface repacking. Sci Rep 2016;6:32153. https://doi.org/10.1038/srep32153.

[56] Humphrey W, Dalke A, Schulten K. VMD: visual molecular dynamics. 27–8 J Mol Graph 1996;14:33–8. https://doi.org/10.1016/0263-7855(96)00018-5.

[57] Still WC, Tempczyk A, Hawley RC, Hendrickson T. Semianalytical treatment of solvation for molecular mechanics and dynamics. J Am Chem Soc 1990;112:6127–9. https://doi.org/10.1021/ja00172a038.

[58] Constanciel R, Contreras R. Self consistent field theory of solvent effects representation by continuum models: introduction of desolvation contribution. Theor Chim Acta 1984;65:1–11. https://doi.org/10.1007/PL00020119.

[59] Phillips JC, Hardy DJ, Maia JDC, Stone JE, Ribeiro JV, Bernardi RC, et al. Scalable molecular dynamics on CPU and GPU architectures with NAMD. J Chem Phys 2020;153:044130. https://doi.org/10.1063/5.0014475.

[60] Klauda JB, Venable RM, Freites JA, O'Connor JW, Tobias DJ, Mondragon-Ramirez C, et al. Update of the CHARMM all-atom additive force field for lipids: validation on six lipid types. J Phys Chem B 2010;114:7830–43. https://doi.org/10.1021/jp101759q.

[61] Jo S, Kim T, Iyer VG, Im W. CHARMM-GUI: a web-based graphical user interface for CHARMM. J Comput Chem 2008;29:1859–65. https://doi.org/10.1002/jcc.20945.

[62] Wu EL, Cheng X, Jo S, Rui H, Song KC, Dávila-Contreras EM, et al. CHARMM-GUI membrane builder toward realistic biological membrane simulations. J Comput Chem 2014;35:1997–2004. https://doi.org/10.1002/jcc.23702.

[63] Jorgensen WL, Chandrasekhar J, Madura JD, Impey RW, Klein ML. Comparison of simple potential functions for simulating liquid water. J Chem Phys 1983;79:926–35. https://doi.org/10.1063/1.445869.

[64] Huang J, Rauscher S, Nawrocki G, Ran T, Feig M, de Groot BL, et al. CHARMM36m: an improved force field for folded and intrinsically disordered proteins. Nat Methods 2017;14:71–3. https://doi.org/10.1038/nmeth.4067.

[65] Best RB, Zhu X, Shim J, Lopes PEM, Mittal J, Feig M, et al. Optimization of the additive CHARMM all-atom protein force field targeting improved sampling of the backbone $\phi$, $\psi$ and side-chain $\chi 1$ and $\chi 2$ dihedral angles. J Chem Theory Comput 2012;8:3257–73. https://doi.org/10.1021/ct300400x.

[66] Huang J, MacKerell AD. CHARMM36 all-atom additive protein force field: validation based on comparison to NMR data. J Comput Chem 2013;34:2135–45. https://doi.org/10.1002/jcc.23354.

[67] Feller SE, Zhang Y, Pastor RW, Brooks BR. Constant pressure molecular dynamics simulation: the Langevin piston method. J Chem Phys 1995;103:4613–21. https://doi.org/10.1063/1.470648.

[68] Martyna GJ, Tobias DJ, Klein ML. Constant pressure molecular dynamics algorithms. J Chem Phys 1994;101:4177–89. https://doi.org/10.1063/1.467468.

[69] Steinbach PJ, Brooks BR. New spherical-cutoff methods for long-range forces in macromolecular simulation. J Comput Chem 1994;15:667–83. https://doi.org/10.1002/jcc.540150702.

[70] Darden T, York D, Pedersen L. Particle mesh Ewald: An N·log(N) method for Ewald sums in large systems. J Chem Phys 1993;98:10089–92. https://doi.org/10.1063/1.464397.

[71] Ryckaert J-P, Ciccotti G, Berendsen HJC. Numerical integration of the cartesian equations of motion of a system with constraints: molecular dynamics of n-alkanes. J Comput Phys 1977;23:327–41. https://doi.org/10.1016/0021-9991(77)90098-5.

[72] Miyamoto S, Kollman PA. SETTLE: an analytical version of the SHAKE and RATTLE algorithm for rigid water models. J Comput Chem 1992;13:952–62. https://doi.org/10.1002/jcc.540130805.

[73] Balusek C, Hwang H, Lau CH, Lundquist K, Hazel A, Pavlova A, et al. Accelerating membrane simulations with hydrogen mass repartitioning. J Chem Theory Comput 2019;15:4673–86. https://doi.org/10.1021/acs.jctc.9b00160.

[74] Hopkins CW, Le Grand S, Walker RC, Roitberg AE. Long-time-step molecular dynamics through hydrogen mass repartitioning. J Chem Theory Comput 2015;11:1864–74. https://doi.org/10.1021/ct5010406.

[75] Feenstra KA, Hess B, Berendsen HJC. Improving efficiency of large time-scale molecular dynamics simulations of hydrogen-rich systems. J Comput Chem 1999;20:786–98. https://doi.org/10.1002/(SICI)1096-987X(199906)20:8<786::AID-JCC5>3.0.CO;2-B.

[76] Noskov SY, Roux B. Control of ion selectivity in LeuT: Two Na+ binding sites with two different mechanisms. J Mol Biol 2008;377:804–18. https://doi.org/10.1016/j.jmb.2008.01.015.

[77] Luo Y, Roux B. Simulation of osmotic pressure in concentrated aqueous salt solutions. J Phys Chem Lett 2010;1:183–9. https://doi.org/10.1021/jz900079w.

[78] Venable RM, Luo Y, Gawrisch K, Roux B, Pastor RW. Simulations of anionic lipid membranes: development of interaction-specific ion parameters and validation using NMR data. J Phys Chem B 2013;117:10183–92. https://doi.org/10.1021/jp401512z.

[79] Smart OS, Breed J, Smith GR, Sansom MS. A novel method for structure-based prediction of ion channel conductance properties. Biophys J 1997;72:1109–26. https://doi.org/10.1016/S0006-3495(97)78760-5.

[80] Smart OS, Neduvelil JG, Wang X, Wallace BA, Sansom MSP. HOLE: a program for the analysis of the pore dimensions of ion channel structural models. J Mol Graph 1996;14:354–60. https://doi.org/10.1016/S0263-7855(97)00009-X.

[81] Jurrus E, Engel D, Star K, Monson K, Brandi J, Felberg LE, et al. Improvements to the APBS biomolecular solvation software suite. Protein Sci 2018;27:112–28. https://doi.org/10.1002/pro.3280.

[82] Lev B, Roux B, Noskov SYu. Relative free energies for hydration of monovalent ions from QM and QM/MM Simulations. J Chem Theory Comput 2013;9:4165–75. https://doi.org/10.1021/ct400296w.

[83] Torrie GM, Valleau JP. Nonphysical sampling distributions in Monte Carlo free-energy estimation: umbrella sampling. J Comput Phys 1977;23:187–99. https://doi.org/10.1016/0021-9991(77)90121-8.

[84] Berselli A, Alberini G, Benfenati F, Maragliano L. The impact of pathogenic and artificial mutations on Claudin-5 selectivity from molecular dynamics simulations. Comput Struct Biotechnol J 2023;21:2640–53. https://doi.org/10.1016/j.csbj.2023.04.001.

[85] Fiorin G, Klein ML, Hénin J. Using collective variables to drive molecular dynamics simulations. Mol Phys 2013;111:3345–62. https://doi.org/10.1080/00268976.2013.813594.

[86] Kumar S, Rosenberg JM, Bouzida D, Swendsen RH, Kollman PA. The weighted histogram analysis method for free-energy calculations on biomolecules. I. The method. J Comput Chem 1992;13:1011–21. https://doi.org/10.1002/jcc.540130812.

[87] Souaille M, Roux B. Extension to the weighted histogram analysis method: combining umbrella sampling with free energy calculations. Comput Phys Commun 2001;135:40–57. https://doi.org/10.1016/S0010-4655(00)00215-0.

[88] Smith LG, Tan Z, Spasic A, Dutta D, Salas-Estrada LA, Grossfield A, et al. Chemically accurate relative folding stability of RNA hairpins from molecular simulations. J Chem Theory Comput 2018;14:6598–612. https://doi.org/10.1021/acs.jctc.8b00633.

[89] Maragliano L, Vanden-Eijnden E. A temperature accelerated method for sampling free energy and determining reaction pathways in rare events simulations. Chem Phys Lett 2006;426:168–75. https://doi.org/10.1016/j.cplett.2006.05.062.

[90] Stoltz G, Vanden-Eijnden E. Longtime convergence of the temperature-accelerated molecular dynamics method. Nonlinearity 2018;31:3748. https://doi.org/10.1088/1361-6544/aac541.

[91] Lesage A, Lelièvre T, Stoltz G, Hénin J. Smoothed biasing forces yield unbiased free energies with the extended-system adaptive biasing force method. J Phys Chem B 2017;121:3676–85. https://doi.org/10.1021/acs.jpcb.6b10055.

[92] Krug SM, Günzel D, Conrad MP, Lee I-FM, Amasheh S, Fromm M, et al. Charge-selective claudin channels. Ann N Y Acad Sci 2012;1257:20–8. https://doi.org/10.1111/j.1749-6632.2012.06555.x.

[93] Qiao B, Jiménez-Ángeles F, Nguyen TD, Olvera de la Cruz M. Water follows polar and nonpolar protein surface domains. Proc Natl Acad Sci 2019;116:19274–81. https://doi.org/10.1073/pnas.1910225116.

[94] Grossfield A. WHAM: the weighted histogram analysis method n.d.

[95] Fuladi S, McGuinness S, Khalili-Araghi F. Role of TM3 in claudin-15 strand flexibility: a molecular dynamics study. Front Mol Biosci 2022;9:964877. https://doi.org/10.3389/fmolb.2022.964877.

[96] Fuladi S, McGuinness S, Shen L, Weber CR, Khalili-Araghi F. Molecular mechanism of claudin-15 strand flexibility. J Gen Physiol 2022;154:e202213116. https://doi.org/10.1085/jgp.202213116.
[97] Li AJ, Nussinov R. A set of van der Waals and coulombic radii of protein atoms for molecular and solvent-accessible surface calculation, packing evaluation, and docking. Proteins 1998;32:111–27.
[98] Yu ASL, Cheng MH, Angelow S, Günzel D, Kanzawa SA, Schneeberger EE, et al. Molecular basis for cation selectivity in claudin-2-based paracellular pores: identification of an electrostatic interaction site. J Gen Physiol 2009;133:111–27. https://doi.org/10.1085/jgp.200810154.
[99] McGuinness S., Li P., Li Y., Fuladi S., Konar S., Sajjadi S., et al. Molecular dynamics analyses of CLDN15 pore size and charge selectivity. bioRxiv 2023: 2023.08.16.553400. https://doi.org/10.1101/2023.08.16.553400.
[100] Sauer DB, Zeng W, Raghunathan S, Jiang Y. Protein interactions central to stabilizing the K+ channel selectivity filter in a four-sited configuration for selective K+ permeation. Proc Natl Acad Sci USA 2011;108:16634–9. https://doi.org/10.1073/pnas.1111688108.
[101] Medovoy D, Perozo E, Roux B. Multi-ion free energy landscapes underscore the microscopic mechanism of ion selectivity in the KcsA channel. Biochim Biophys Acta Biomembr 2016;1858:1722–32. https://doi.org/10.1016/j.bbamem.2016.02.019.
[102] Furini S, Domene C. Selectivity and permeation of alkali metal ions in K+-channels. J Mol Biol 2011;409:867–78. https://doi.org/10.1016/j.jmb.2011.04.043.
[103] Furini S, Domene C. Computational studies of transport in ion channels using metadynamics. Biochim Biophys Acta 2016;1858:1733–40. https://doi.org/10.1016/j.bbamem.2016.02.015.
[104] Roux B. Ion channels and ion selectivity. Essays Biochem 2017;61:201–9. https://doi.org/10.1042/EBC20160074.
[105] Kopec W, Rothberg BS, de Groot BL. Molecular mechanism of a potassium channel gating through activation gate-selectivity filter coupling. Nat Commun 2019;10:5366. https://doi.org/10.1038/s41467-019-13227-w.
[106] Gu R-X, de Groot BL. Central cavity dehydration as a gating mechanism of potassium channels. Nat Commun 2023;14:2178. https://doi.org/10.1038/s41467-023-37531-8.
[107] Fowler PW, Abad E, Beckstein O, Sansom MSP. Energetics of multi-ion conduction pathways in potassium ion channels. J Chem Theory Comput 2013;9:5176–89. https://doi.org/10.1021/ct4005933.
[108] Alberini G, Benfenati F, Maragliano L. Structural mechanism of ω-currents in a mutated Kv7.2 voltage sensor domain from molecular dynamics simulations. J Chem Inf Model 2021;61:1354–67. https://doi.org/10.1021/acs.jcim.0c01407.
[109] Alberini G, Alexis Paz S, Corradi B, Abrams CF, Benfenati F, Maragliano L. Molecular dynamics simulations of ion permeation in human voltage-gated sodium channels. J Chem Theory Comput 2023;19:2953–72. https://doi.org/10.1021/acs.jctc.2c00990.
[110] Beckstein O, Biggin PC, Sansom MSP. A hydrophobic gating mechanism for nanopores. J Phys Chem B 2001;105:12902–5. https://doi.org/10.1021/jp012233y.
[111] Zhu F, Hummer G. Drying transition in the hydrophobic gate of the GLIC channel blocks ion conduction. Biophys J 2012;103:219–27. https://doi.org/10.1016/j.bpj.2012.06.003.
[112] Roth R, Gillespie D, Nonner W, Eisenberg RE. Bubbles, gating, and anesthetics in ion channels. Biophys J 2008;94:4282–98. https://doi.org/10.1529/biophysj.107.120493.
[113] Rao S, Lynch CI, Klesse G, Oakley GE, Stansfeld PJ, Tucker SJ, et al. Water and hydrophobic gates in ion channels and nanopores. Faraday Discuss 2018;209: 231–47. https://doi.org/10.1039/C8FD00013A.
[114] Flood E, Boiteux C, Lev B, Vorobyov I, Allen TW. Atomistic simulations of membrane ion channel conduction, gating, and modulation. Chem Rev 2019;119: 7737–832.